Multi-Technique Investigation of Extruded Clay Brick Microstructure

Konrad J.Krakowiak[(1)], Paulo B. Lourenço[(1)], Franz Josef Ulm[(2)*]

[(1)]University of Minho, ISISE, Department of Civil Engineering, Azurém, 4800-058,Guimarães, Portugal

[(2)]Massachusetts Institute of Technology, Department of Civil & Environmental Engineering, Cambridge, MA, 02139, USA

ABSTRACT

Despite the omnipresence of clay brick as construction material since thousands of years, fundamental knowledge about the link between composition, microstructure and mechanical performance is still scarce. In this paper, we employ a variety of advanced techniques of experimental mechanics and material characterization for extruded clay brick for masonry, that range from Scanning Electron Microscopy (SEM) coupled with Energy-dispersive X–ray Spectroscopy (EDX), Mercury Intrusion Porosimetry (MIP), to Instrumented Nanoindentation and macroscopic strength and durability tests. We find that extruded clay brick possesses a hierarchical microstructure: depending on the firing temperature, a “glassy” matrix phase, which manifests itself at sub-micrometer scales in form of neo-crystals of mullite, spinel-type phase and other accessory minerals, forms either a granular or a continuum matrix phase that hosts at sub-millimeter scale the porosity. This porous composite forms the backbone for macroscopic

*Corresponding Author: ulm@MIT.EDU, Tel: 1-617-253.3544; Fax: 1-617-253.6044

material performance of extruded brick, including anisotropic strength, elasticity and water absorption behavior.

1 INTRODUCTION

Clay brick, whose origin can be traced back to around 4300BC,[1] still finds wide use in today's building industries. Next to concrete and steel, masonry is the most used construction material on Earth. Infill panels, masonry veneer and low-rise structural masonry buildings are common applications of clay brick.[2] However, in contrast to other construction materials (cement-based materials, metallic materials, polymer-based composites etc.), the implementation of the engineering science approach for masonry has lagged behind, creating an increasing gap between wide-spread use and fundamental understanding of masonry. With a focus on linking the mechanical performance and durability of contemporary masonry materials with basic constituents present at different scales, the overall goal of this paper is to contribute to filling this gap.

In order to reach this goal, we present results from an extensive experimental campaign targeted at the detailed characterization of clay brick over seven orders of magnitude (from 10^{-9} m to 10^{-2} m), which includes elemental and phase composition, microstructure investigations, and mechanical property characterization at nano and macro-scales. The elemental and phase composition is determined with the aid of Energy-dispersive X-ray Spectroscopy (EDX), and X-ray Diffraction (XRD). The extensive use of Scanning Electron Microscopy (SEM) on the polished sections of ceramics allows the capturing of microstructural features, from a scale of tens of nanometers to hundreds of micrometers. Additionally, Mercury Intrusion Porosimetry (MIP) combined with Digital Image Analysis (DIA) of SEM images proves to be a beneficial mean to characterize pore size distribution, void shape and alignment, as well as

interconnectivity. Furthermore, the mechanical properties of this heterogeneous material are investigated with the aid of instrumented nano-indentation reinforced with massive grid indentation technique,[3,4] in addition to conventional uniaxial compression tests at macro-scale. These results are synthesized into a multi-scale model of brick, which allows one to pin down the effect of composition and processing on macroscopic material performance.

2 MATERIALS

The investigated materials represent two types of solid brick commonly employed in the construction industry; facing brick (labeled B1) and general use common brick (labeled B2). The facing brick is manufactured in a fully automated fashion. It is fired inside a gas fuelled tunnel kiln for a ~55 hrs firing cycle duration. Maturing of the ware is achieved at 1030ºC for about 5.5 hrs. The second type of brick, B2, is an example of a building ceramic which has been produced with a more traditional technology. The green ware is dried in semi-open space above running annular kiln of Hoffman type construction. The kiln's chambers are charged with the dried, green brick, which then is fired to the maximum temperature of 950-980ºC. The cycle from cold-to-cold takes 72 hrs, with a maturing time of ~7.5 hrs. Both types of investigated brick are shaped with soft extrusion technique (B1-along the height or parallel to the bed face, B2-along the length or parallel to the head face) to attain standard brick dimensions 24×11.5×6.5 cm. Raw materials for the production of bricks B1 and B2 present chemical (Table 1) and mineralogical similarities (see Fig. 1), with kaolin (K) and muscovite (M) as the main clay mineral species, together with K-feldspar microcline (Kf) and some traces of plagioclase series (Pf) in B1, quartz (Q) and accessory minerals, such as hematite (H), rutile and calcite (C) (<3 wt.% in sample B1).

3 METHODS AND RESULTS

3.1 PHASE IDENTIFICATION

The characteristic feature of structural ceramic materials is their complexity with respect to the number of incorporated phases, as well as its microstructural arrangement. The first aspect may be quite accurately resolved with the aid of XRD, which is well known in the earth sciences and other fields.[5,6] For this purpose, the samples of investigated materials B1 and B2 have been prepared, in the form of powder passing the standard sieve ASTM No.230, as well as polished sections of bulk solids. Six powder samples and three polished samples for each type of brick were investigated in the Bruker D8 Discover diffractometer, with conventional Bragg-Brentano geometry, and cupper radiation CuKα. The spectra has been collected over 2θ intervals ranging from 5º to 70º degrees, with step size 0.05º and time step 3 sec. The phase matching has been carried using the standard patterns included in the database of The International Center for Diffraction Data (ICDD).

Both types of investigated brick are composed of common phases: α-quartz (Q), K-feldspar (Kf), hematite (H) and mullite (Mu). Mullite seems to be more abundant in the B1 sample, even if its traces are also recorded in the B2 sample (see Fig. 2). This result is due to the higher temperature applied in the firing of the facing brick, which is above 980ºC, considered as the point of formation of γ-Al_2O_3 spinel-type phase (S) accompanied by mullite development from melting kaolinite and muscovite clay minerals.[7,8,9,10] Hence, it is not surprising that the muscovite mineral is still easily detected in the B2 sample with the lower processing temperature. The significant amount of the background signal can be attributed to the presence of an amorphous phase, e.g. aluminosilicate glass. The contribution of this non-crystalline solid to the brick microstructure increases with the temperature, and spans from around 10% in weight for brick fashioned at 900°C to as much as 40% for processing temperature of 1100°C. [11,12]

The results of this qualitative analysis are supported by the results of EDX elemental mapping on polished sections of bulk samples. Distribution maps of silicon (Si), aluminum (Al) and other incorporated elements were collected, and the regions close to the theoretical composition of quartz (red), feldspar (dark blue) and hematite (violet) could be identified (see Fig. 3). The 'binding phase' (green and yellow) is a composite of crystals of mullite and spinel-type phase embedded in the glass (sample B1). However, the geometrical forms of these minerals could not be obtained in this analysis, because of the fine character of the crystal structures of sub-micron size as well as the presence of hosting glass. The features of this size are below the spatial resolution limit which is rarely much better than 1μm in this type of analysis[13] and is implied by the volume of the material probed with the electron beam in EDX coupled to conventional SEM microscope.

This phase identification analysis reveals, in a simple manner, how the brick processing temperature can affect its mechanical and physical performance. The mechanical strength and stiffness may be expected to be higher in sample B1, since the relatively weak backbone of the compacted green ware composed of the clay minerals has been transformed into a stronger one made of mullite and spinel crystals mainly wrapped in amorphous glass. In contrast, sample B2 tends to preserve still the original internal structure, since the phase transformation process has not been fully accomplished and a large fraction of clay minerals is still detectable. Coarse particles of quartz and feldspar in both materials tend to be the filler, akin to gravel aggregates in concrete.

3.2 MICROSTRUCTURE

Prior to the investigations of the microstructure, a minimum of three samples for each type of brick were cored (along the shortest edge of the brick) from the central part of the solid unit, and

the polished sections were prepared. The preparation procedure includes: impregnation under vacuum with low viscosity epoxy resin EpoThin Buehler, coarse grinding on the diamond disc 45μm Apex DGD Buehler; fine polishing with water based diamond suspensions grade 9μm, 3μm and 1μm applied on perforated pad TexMetP Buehler. In the last pass, a 0.25μm oil based diamond suspension grade, in exchange with colloidal silica, was occasionally used during a short duration. The surfaces oriented along the length, width and height of the brick were exposed to microscopic examination. A minimum of 12 images for each magnification step (×100≈1238×925 μm, ×200≈619×463 μm, and ×400≈310×231μm, image resolution 712×484, and 3584×3301 pixels) was acquired on the surface at randomly selected locations, with the Backscattered Electron Detector (BSEM). Qualitative and quantitative analysis of the porous domain was carried out on normalized binary images constructed via the automatic thresholding procedure proposed by Otsu,[14,15] and implemented into ImageJ, a non-commercial image analysis package.[16]

Additionally, to resolve the nano-crystals of mullite and other phases existing within the binding matrix of brick B1, and the aggregates of molten clay structures existing within brick B2, chemical etching with 6% hydrofluoric acid HF was carried out for 1 min. to 4 min. prior to SEM imaging.

The experimental micrographs expose, at different length scales of observation, the dominant features of the microstructure of B1 and B2 samples. Both microstructures converge to a common pattern at larger length scales. On the other hand, the building blocks present at the lowest level considered here ($<10^{-6}$ m) diverge significantly, preserving only the chemical similarity. Hence, each material is characterized by a different type of matrix phase (see Fig. 4(a-b) and Fig. 5(a-b)), which hosts larger scale components.

More specifically, the matrix of facing brick B1 is a composite of amorphous glass, crystals of primary mullite (PM) and occasional acicular forms of secondary mullite (SM), spinel-type phase and hematite (H) (Fig. 6a). The size of incorporated crystals varies from nano- to micrometer depending on mineralogy of raw materials and processing conditions, as revealed in transmission electron studies (TEM) carried out by other researchers.[8,9,17,18,19] In contrast, the main matrix components of the B2 sample are porous complexes of dehydroxylated and partially molten clay particles (Fig. 6b), together with rare local clusters of glass reinforced by early developed nano-crystals. The matrix in the B2 sample is reminiscent of the green ware (Fig. 5(b)), while a complete new structure has been developed in sample B1 upon firing (Fig. 4(b)). Otherwise said, there is a clear structural difference in matrix for the brick microstructure as a consequence of the firing process (temperature and duration). This observation suggests that the response of both microstructures (materials) to prescribed physical and mechanical loads is expected to be different, due to the different forms of the matrix present in the two types of clay brick.

The composite matrix phase discussed before is an inherent structural element of the microstructure at larger scales, $10^{-6} < l < 10^{-4}$ m. At this level new components of the brick microstructure become relevant, namely micro-porosity and aggregates of silt. The difference in the characteristics of micro-porosity can be directly observed on the SEM micrographs previously shown (Fig. 4(a) and 5(a)), and can be quantified with the aid of DIA technique, MIP and standard gravimetric and capillary suction methods (Table 2).

The volume occupied by the voids in both samples is comparable with slight increase in sample B2, but the pore size distributions curves obtained by DIA exhibit different modality and different location of the modes (see Fig. 7(a)). The porosity in sample B1 exhibits a unimodal distribution with the mode located at $d_{eq} \approx 18$ μm, and a negative skew where voids tend to concentrate toward larger equivalent diameters (log-normal distribution). The voids of this

sample are within an interval of 1 to 100 μm. In contrast, the porosity domain within the microstructure of sample B2 exhibits higher variability of voids with respect to the assumed equivalent diameter. In this case, a clear bimodality is encountered, which represents two families of pores separated by one order of magnitude in size, $d_{eq,I} \approx 3$ μm and $d_{eq,II} \approx 30$ μm. In addition, the entire pore distribution is inscribed within a significantly larger domain. Pores with diameters of hundreds of nanometers seem to occupy a non-negligible fraction of the total porosity. According to this analysis, sample B1 represents a coarser and more uniform porosity distribution, while a more refined structure with larger variation is observed for sample B2.

This significant difference between the microstructure of the investigated bricks at the intermediate material scale is confirmed by mercury intrusion investigation (Fig. 7(b-c)). Carried out in low and high pressure regimes with AUTOPORE IV 9510, Micromeritics, six specimens of each sample with an average dried mass of 7.5 g and volume 3.6 cm^3 were studied on the single intrusion-extrusion cycle up to the maximum pressure of 100 MPa and an equilibration time of 10sec. The MIP results on intrusion confirm the difference in modality for the two samples, as well as the tendency of B1 sample towards a coarser porous domain than the one incorporated within B2 brick. Similar observation is given by the MIP drainage results, although the bimodality becomes less apparent in this case for brick B2. Despite the qualitative good agreement of MIP and DIA analysis, there exists an evident discrepancy between them, due to the different location of the modes. The peaks obtained on intrusion cycle as well as the entire distribution tend to shift towards smaller diameters.[22] Such a bias which is also referred to as the 'ink bottle effect', occurs when the void to be filled with intruding mercury encounters narrow throats, leading to the misrepresentation of the pore as having the diameter of its throats, see Abell et al.[23] for a description of this phenomenon in complex microstructures of cement-based materials.

The last feature of the micro-porosity domain to be discussed here, at observation scale $10^{-6} < l < 10^{-4}$ m, is the preferential orientation along one specific direction. This effect has been observed more pronounced in the B1 sample under the SEM microscope (see Fig. 4(a)), and may be attributed to the technology of brick shaping by extrusion at the green stage. In this process, the plastic mass is forced through a die that is placed in the end of the pressure head of the extruder, leading to the development of interlaminar tangent stresses. These stresses provoke alignment of the irregular particles along streamlines, and the occurrence of laminations in the green ware (Fig. 8). Simultaneously, the air pockets present within the plastic body due to the insufficient vacuum inside the de-airing chamber, adopt a scalene ellipsoidal form, with dominant axis aligned with the extrusion direction.

The results from water absorption experiments by capillary action, carried out independently for each different direction, corroborate the microstructural signature related to the extrusion technique. In this setup each cylindrical core ϕ=2.5 cm and h=5.0 cm (six cores for each direction) are brought in contact with water through its bottom face, and the mass of absorbed water is monitored over time.[20]

The weight change behavior of both samples shows a significant difference with respect to the orientation (see Fig. 9(a-b)): samples cored along the direction of extrusion present the highest sorptivity (S) and significantly diverge from the two other groups ($S_z/(S_y,S_x)\approx1.5$ for B1, $S_y/(S_x,S_z)\approx1.4$ for B2), in which the trend in water absorption appears to be quite similar ($S_x/S_y\approx1$ for B1, $S_x/S_z\approx1$ for B2). The movement of water within the system of micro-voids is considerably facilitated along the extrusion direction. Such phenomena may occur if the microstructure of the material exhibits an aligned porosity with enhanced interconnectivity, or a laminar microstructure (see Fig. 4(a) and Fig. 8). Features of this type effectively increase the rate of water movement along direction of the alignment (see Fig. 10(a-b)).

Finally, at larger scales, $l > 10^{-4}$ m, SEM images confirm features identified previously by other researchers,[26,27] namely, the presence of coarse aggregates associated with inherent fissures, as well as discontinuities at the interface of coarse aggregates and glassy matrix, together with large meso-voids (cracks). The cracks have been attributed to the volume contraction during phase transformation of quartz from its β- form to the more stable at room temperature α-form, while the discontinuities at the boundaries have been considered to result from the mismatch in thermal expansion coefficients between quartz and composite of glassy matrix, silt grains and micro-porosity.

3.3 MECHANICAL PERFORMANCE

Following the analysis of phase composition and microstructural features, the effect of composition and microstructure on the mechanical performance of the investigated brick samples is addressed using a combination of classical macroscopic strength tests and nanoindentation tests.

Macroscopic compressive strength $f_{c,i}$ and modulus of elasticity E_i of both materials in three directions $i=X,Y,Z$ (see Table 3) were obtained by standard compression tests on cylindrical samples with a height to ratio diameter of two ($h/D=2$). A minimum of 12 tests was carried out in each direction according to the procedure adopted from.[28] Note that it is normal practice to report the macroscopic compressive strength of brick, which is a basic and much used material property for mechanical characterization, even if the values in different directions are not usually reported.

As expected, the results (Table 3) show that facing brick type sample B1 has significantly higher mechanical properties than the common brick B2. For instance, the maximum strength capacity of B2 is ≈56 MPa, compared to a strength capacity of ≈83 MPa for B1, which are values

within the expected range for solid clay brick. Due to the high strength, both materials exhibit rather brittle failure at the strength limit.

A similar trend is observed for the modulus of elasticity, although reported values may be somewhat reduced due to the compliance of the experimental setup. In agreement with results reported by Oliveira et al.,[29] the highest strength and modulus are found along the axis aligned with the direction of green body extrusion. The performance of both materials in directions perpendicular to the extrusion direction is quite similar. This suggests that extruded bricks exhibit at macroscopic level (at least) transverse isotropic elastic behavior characterized by five elastic constants.[30]

The macro-scale mechanical behavior is inherently linked to microstructure and constituent properties at nano- and micro-scale. In order to quantify this link, the best experimental technique able to assess mechanical properties at the smallest and intermediate material scales is instrumented indentation,[31] employed in form of massive grid indentation technique.[32] This testing procedure, which originates from the traditional hardness measurement developed by Brinell,[33] is based on the continuous monitoring of the load and displacement of the hard probe as it is driven and withdrawn from the material at discrete locations of a grid $l_x \times l_y$ that spans a specific region on a material surface $L_x \times L_y$ (Fig 11(a-c)). The obtained load-displacement diagrams (Fig 11(a)) allow the determination of the material hardness H_i and indentation moduli M_i (Fig 11(b)) at each location (Fig 11(c)), based on the contact area at maximum load and initial unloading stiffness.[34,35]

In case of composite materials, the i-th node record of hardness and indentation modulus, $x_i=[H_i;M_i]$, may belong to one j=1…n of n mechanically active phases G_n with average properties $(\bar{H}_j;\bar{M}_j)$. Hence, the statistical analysis (deconvolution) that is carried out on the grid dataset (Fig 11(b)) aims at estimating the number of statistically significant phases, as well as their vectors of

mean properties with covariance matrices $\varphi_j=[\mu_j,\Sigma_j]$ and associated fractions π_j. Recent literature reports a variety of deconvolution strategies applied for this purpose.[4,32,36] We employ here a multivariate mixture model to identify the number of phases and phase properties. Based on the Finite Gaussians Mixture Model (FGMM) (Eq. 1.1 and Eq. 1.2),[37,38] the estimation of the parameters is carried out according to the Maximum Likelihood (ML) function, via the Expectation Maximization (EM) algorithm[39], with the aid of non-commercial program called EMMIX developed by Peel and McLachlan.[38,40]

$$f(\mathbf{x};\boldsymbol{\psi}) = \sum_{j=1}^{n} \pi_j f_j(\mathbf{x};\boldsymbol{\varphi}_j) \tag{1.1}$$

$$\sum_{j=1}^{n} \pi_j = 1,\ \pi_j \geq 0 \tag{1.2}$$

The applicability and efficiency of this experimental approach and statistical analysis technique with reference to clay brick is briefly presented next and discussed on the basis of results (Fig.12(a-d)) selected from the experimental campaign on facing brick B1.

The porous samples were impregnated with epoxy resin prior to indentation testing. This resin impregnation was employed in order to facilitate the preparation of a smooth surface by the polishing process, and to be able to identify porosity by contact experiment due to a significant lower hardness of the solidified epoxy resin (H≈0.3GPa) compared to the hardness of the 'glassy' matrix, quartz and other incorporated phases. However, this mismatch in hardness and required prolonged polishing time may provoke a rounding of edges of hard phases or their removal, which may entail some ill-conditioned measurements. A fine statistical analysis is required to identify and isolate such tests from the overall analysis.

The qualitative picture regarding the phases within the investigated region in this particular analysis is given by the BSEM micrograph (Fig. 12(a)). Three main components can be distinguished (confirmed by EDX analysis), namely, silt aggregates (quartz), 'glassy matrix' and porosity filled with hardened epoxy resin. Each of the components has distinct mechanical properties. However, while the hardened epoxy resin and quartz may be considered as homogeneous phases at this scale, the 'glassy matrix' developed within facing brick B1 is a composite material, in which fine nano-crystals of mullite and other accessory minerals are incorporated and are bonded by aluminosilicate glass.[17,18,41,42]

In the chosen experimental setup the indentation mesh spans a region $L_x \times L_y = 60 \times 54$ μm and includes $N \times M = 41 \times 37$ indentation points. The indentations with Berkovich diamond tip are force controlled, with a maximum force of P=2.25 mN provoking penetration depths between ≈130 nm for hard grains and ≈700 nm for soft epoxy filling the pores. The CSM nanoindentation tester equipped with the temperature and moisture controlled enclosure has been used. The statistical deconvolution of the data in the form 'as received' (including abnormal measurements) is presented in the form of a scatter diagram in the H-M plane (Fig. 12(d)) together with simultaneous allocation of data into statistically significant groups. Using a Bayesian Information Criterion (BIC),[43] it is possible to identify a minimum value of BIC for seven normal components.

The first four clusters have mean hardness and indentation moduli significantly lower than the rest. Such statistically significant phases are associated with indentation on pores filled by epoxy. In contrast, the remaining three clusters represent indentations on (i) the bulk 'glassy' matrix, H_5=9.9 GPa, M_5=87.3 GPa, and (ii) different aggregates of quartz, H_6=13.4 GPa, M_6=88.6 GPa and H_7=14.5 GPa, M_7=103.4 GPa. This hypothesis is validated by the microstructural phase map shown on BSEM image and its statistical reproduction based on a cluster analysis of the

indentation data, subjected to direct comparison (Fig. 12 (a-b)). According to this analysis, the aggregates of quartz are properly recognized (red and orange), as well as the group of indents that represent the binding matrix (yellow). Additionally, it is noticed that the experimental records allocated to the first four groups are linked to pores intruded by epoxy. In turn, this group may also include some abnormal measurements (imperfect contact detection, fracture etc.), which in general fall in the lower range of measured quantities.

To confirm the initial conclusions, a filtering of experimental data was carried out with respect to the possible deviations from continuous load-displacement curves $P \propto h^m$,[34] which typically point to degenerated measurements such as fracture under the indenter, soft-on-hard behavior or other anomalies (Fig. 13(a-c)). The filtered dataset was then deconvoluted again using the described cluster algorithm (Fig. 13(d-e)). The following main observations may be drawn: the group of records with the lowest hardness and modulus is enlarged leading to a shift in the vector of mean properties H_1=0.3→0.4 GPa and M_1=17.5→20.0 GPa, and the families G_2 and G_3 previously indentified are absent in the deconvolution of the filtered data set. Hence, the data of these two groups establish a statistically significant set, which was identified in the original analysis. Moreover, next to the rare events on grains of quartz and matrix, the set of ill conditioned indentation events includes mostly the ones located within the void domain in close proximity (boundary zone) of the 'glassy' matrix or quartz (see Figs 12(b) and 13(d)). The latter groups do not experience significant alterations in mean properties as well as allocation of the records upon data filtering.

The experimental indentation modulus of the quartz phase obtained from this analysis appears to be very close to the stiffness values (C_{33}≈106 GPa and C_{11}≈87 GPa)[44] reported in the literature for single crystal of quartz. The first of the mean values M_6≈87GPa associated with the quartz phase approaches C_{11} and is around 10% higher than Young's modulus in this direction

E_{11}≈79GPa, while the second M_7≈103GPa is just slightly lover than C_{33}, but becomes equal to E_{33}≈103GPa. Additionally, the average value of both means is in close proximity of the Voight-Reuss-Hill average E_{pol}≈99GPa.[44] However, it must be emphasized at this point that the indentation modulus M for crystal materials is considered to represent some average of elastic constants, which additionally depends on the orientation of the indented surface with respect to the material axes.[34,45] Therefore, it does not correspond directly to any of the referred stiffness values. The measured hardness of quartz is consistent with literature hardness $H_{(001)}$≈13÷14 GPa.[34] Estimated mechanical properties of the 'glassy' matrix, H_3≈10 GPa, M_3≈85 GPa, are larger than values reported for soda-lime-silica glass (H≈6 GPa, E≈70 GPa→M≈74 GPa)[34] and fused silica (H≈8 GPa, E≈72 GPa→M≈74 GPa)[34]. On the other hand, comparing with the properties of aluminosilicate glass (H_V≈6 GPa→H≈6.5 GPa, E≈89 GPa→M≈94 GPa)[33] the hardness of matrix is still significantly higher, but its stiffness appears to be lower. These enhanced mechanical properties may be attributed to the presence of nano-crystals within the 'glassy' matrix, as well as to the multi-component character of incorporated glass.[17,41] It is known that the incorporation of alkali oxides or iron as well as reduction in silica content within the matrix may alter hardness and modulus of glass, e.g. basaltic glass (H≈8.6 GPa, M≈97 GPa)[46,47].

Finally, it is worth mentioning that the resultant indentation (see Fig. 12(c)) depth h≈200 nm on the 'glassy' matrix phase activates an interaction volume of a characteristic size d=3h-5h=0.6-1.0 μm.[48] Hence, d appears to be between three and five times larger that the nano-crystals of primary mullite, hematite and spinel, for which the maximum size of observed crystals in sample B1 seems to be d_0^1≈200 nm, up to two times larger than the size of acicular crystals of secondary mullite d_0^2≈500 nm. The secondary type is occasionally observed within large pockets of the 'glassy' matrix rich in alkaline impurities, causing excessive growth of this needle shaped form.

Studies carried out by other researchers[17,41,42] confirm this observation, and specify the limiting size of primary mullite derived from kaolinite and muscovite clay as being <100 nm, and as being <1μm for secondary mullite. Given this size, it is unlikely that nanoindentation operated to a depth h≈200 nm will be able to actually probe "pure" properties of primary or secondary mullite as well as glass, but rather a composite response that may include effects of fine-scale porosity.

4 DISCUSSION

The complexity of clay brick microstructure requires the use of a multi-technique approach to identify the link between chemical and mineralogical composition, microstructure and mechanical performance. The results presented in this paper provide new insight into the multi-level and multi-component morphology of these silica and alumina rich ceramic material systems, which can be associated with distinct materials scales (Fig. 14), as detailed next.

Level "0" (<10^{-5}m)

A good starting point for the multi-scale structure of brick is the "glassy" matrix phase, which manifests itself at sub-micrometer scales in form of neo-crystals of mullite, γ-Al_2O_3 spinel-type phase and other accessory minerals. Such crystals, qualitatively identified with XRD, may reach hundreds of nanometers in size. As the SEM microscopy study on chemically etched sections revealed, these crystals are present in different geometrical forms, from cubic structures like in case of primary mullite and hematite, to acicular forms in the case of secondary mullite. These crystals are hosted by an amorphous phase, and form a nano-composite with chemical and mechanical similarity to aluminosilicate glass with addition of alkaline oxides, as revealed by EDX analysis and instrumented grid indentation. Such a composite tends to develop upon the application of temperatures significantly above 950°C, and is present in the microstructure of the

facing brick type B1. For lower temperatures, dehydroxylated muscovite was still observed in the diffraction spectra of B2 brick, which suggests that the phase transformation was not completed. Further studies of this material based on SEM micrographs confirm this hypothesis, exposing significant fraction of residual, partially molten clay particles assembled in aggregates, next to the initial 'glassy' melt. So observed clay aggregates within B2 sample tend to form 'grains' defined here as 'grains type A', whereas the early developed polycrystalline-amorphous matrix in the regions of high chemical potential are specified as 'grains type B' (Fig. 14).

Level "I": Primary Brick (<10^{-4}m)

At sub-millimeter scale, matrix and porosity form a porous composite material whose behavior drives much of the macroscopic performance of clay brick materials. We therefore coin this scale as the "Primary Brick" scale. Depending on processing temperature and level "0" morphology, the structure of the "Primary Brick" may possess either a disordered granular morphology or a continuous matrix morphology with pore inclusions: the granular morphology is characteristic of brick B2, composed of level "0" grains (type A and B) and silt particles; a continuous matrix morphology is characteristic of the high-temperature fired facing brick B1, which possesses a continuous polycrystalline-amorphous binding matrix with silt and pore inclusions. These two morphological forms are inherently related to the porosity that dominates this scale, and which, according to results of MIP, DIA and gravimetric methods, may occupy up to one-third of the bulk material.

MIP and DIA results indicate that the micro-porosity spans a large range of scales from hundreds of nanometers to tens of micrometers, with modes clearly defined. A broad pore distribution is present in sample B2, which was produced at a temperature close to the melting temperature. The clear modes in the pore-size distributions are indicative of a coarse porosity

development that can be attributed to the proximity of the firing temperature and the melting temperature. On the other hand, a significant fraction of fine voids is also found reminiscent of an inter-granular porosity incorporated between the remnants of clay particles.

Another important feature which is encountered in this morphology is the preferential orientation of voids, which are rarely spherical. This feature of the porosity is attributed to the extrusion technique employed to shape the brick at its green stage. In fact, forming of the material in the extruder tends to align irregular particles and to alter the form of originally spherical voids. As a result, the coarse porosity that builds up on the expense of smaller void coalescence tends to align along the extrusion direction, which affects physical and mechanical properties at macro-level. This alteration has been independently demonstrated in water absorption tests and macro-mechanical tests, in which respectively the capillary water uptake, the Young's modulus and the strength, measured along the different material axes, show strong evidence of a macroscopic anisotropic behavior.

Level "II": Secondary Brick (<10^{-2}m)

The top level of the proposed hierarchical material description is defined by the "Secondary Brick" structure, which is common for both materials B1 and B2. At this sub-centimeter scale, the "Primary Brick" composite hosts fractured grains of coarse sand, discontinuous interface and possibly meso-voids. The discontinuity at the interface of the sand particles can be attributed to the thermal mismatch between host matrix and sand (mostly quartz) grains.

5 CONCLUSIONS

It has been demonstrated, that extruded clay brick is a complex ceramic system with a hierarchical microstructure. The multi-scale nature of this composite can be dissected into three

scales: Level “0” ($<10^{-5}$ m), “Primary Brick” ($<10^{-4}$ m) and “Secondary Brick” ($<10^{-2}$ m). Depending on the brick firing temperature, the level “0” represents the nano-composite of “glassy” matrix, or assembly of dehydroxylated, partially molten clay aggregates and initial melt. The “glassy” matrix tends to develop in the brick fired at temperatures significantly above melting temperature of the raw clay minerals. This temperature assures the formation of the amorphous binding phase, as well as crystallization of primary and secondary mullites, hematite and other accessory minerals in the nanometers size, as revealed by XRD and SEM micrographs studies. These crystal phases tend to enhance the hardness of the “glassy” matrix; but it leaves the measured elastic properties in close proximity to that of the aluminosilicate glass, as demonstrated by instrumented grid indentation technique. The structure of “Primary Brick” is defined at sub-millimeter scale, where matrix, silt and porosity form a porous composite, whose behavior drives much of the macroscopic mechanical and physical performance of extruded brick. Depending on both the morphology at level “0” and the processing temperature, the structure of the “Primary Brick” exhibits either a granular morphology or continuous matrix morphology with pore inclusions. The granular morphology with finer micro-porosity prevails when the firing temperature approaches the melting temperature, whereas the continuous morphology with coarser voids is inherent to bricks fashioned at significantly higher temperatures. Due to shaping technology of the green brick by extrusion, the micro-porosity exhibits a preferential orientation along the extrusion direction. Therefore the water suction along this specific path is significantly enhanced compared to the other two orthogonal directions. A similar trend has been observed for the modulus of elasticity and strength, and suggests that extruded brick at macroscopic level follows (at least) transverse isotropy. The top level in the proposed hierarchical description represents the structure at sub-centimeter scale of “Secondary Brick”. The fractured coarse aggregates of sand, as well as peripheral cracks at the interface of

the coarse particles and the composite represented by “Primary Brick” are the main microstructural features at this material scale.

The results of the multiscale technique thus applied to brick shed new light on the complex interplay at multiple scales between composition, processing and macroscopic performance of masonry materials. This should make it possible, in the close future, to fine tailor this omnipresent construction material for specific use and performances.

ACKNOWLEDGMENTS

Authors gratefully acknowledge Portuguese Foundation for Science and Technology (FCT) for providing doctoral scholarship under the reference SFRH/BD/39232/2007 for Konrad J. Krakowiak. Special thanks to Dr. J. P. Castro Gomes, Centre of Materials and Building Technologies (C-MADE), University of Beira Interior for making feasible Mercury Intrusion measurements, as well as Dr. G. P. Souza for helpful guidance and advices related to this work.

REFERENCES

[1]H. Reh, “Current classification of ceramic materials,” pp. 39-62 in Extrusion in Ceramics, Engineering Materials and Processes. Edited by F. Händle. Springer-Verlag Berlin Heidenberg, 2007.

[2]P. B. Lourenço, “Computational strategies for masonry structures”, Doctoral Thesis, Delft University of Technology, 1996.

[3]G. Constantinides, “Invariant mechanical properties of calcium-silicate-hydrates (C-S-H) in cement-based materials: Instrumented nanoindentation and microporomechanical modeling”, Doctoral Thesis, Massachusetts Institute of Technology, 2006.

[4]F.-J. Ulm, M. Vandamme, C. Bobko, J.A. Ortega, K. Tai, C. Ortiz, "Statistical Indentation Techniques for Hydrated Nanocomposites: Concrete, Bone and Shale," J. Am. Ceram. Soc., 90[9] 2677-2692 (2007).

[5]G. W. Brindley, G. C. Brown, "Crystal structures of clay minerals and their X-ray identification," Mineralogical Society of Great Britain & Ireland, 1984.

[6]V. K. Pecharsky, P. Y. Zavalij, "Fundamentals of Powder Diffraction and structural characterization of materials", Springer, 2005.

[7]G. W. Brindley, M. Nakahira, "The Kaolinite-Mullite reaction series: III, the high temperature phases," J. Am. Ceram. Soc., 42[7] 319-324 (1959).

[8]B. Sonuparlak, M. Sarikaya, I. A. Aksay, "Spinel phase formation during 980°C exothermic reaction in the Kaolinite-to-Mullite reaction series," J. Am. Ceram. Soc., 70[11] 837-42 (1987).

[9]K. Srikrishna, G. Thomas, R. Martinez, M. P. Corral, S. de Aza, J. S. Moya, "Kaolinite-mullite reaction series: a TEM study," J. Mater. Sci., 25 607-612 (1990).

[10]S. G. Barlow, D. A. C. Manning, "Influence of time and temperature on reactions and transformations of muscovite mice," Br. Ceram. Trans., 98[3] 122-126 (1999).

[11]M. Dondi, M. Marsigli, I. Venturi, "Microstructure and mechanical propoerties of clay bricks: comparison between fast firing and traditional firing," Br. Ceram. Trans., 98[1] 12-18 (1999).

[12]G. Cultrone, E. Sebastián, K. Elert, M. J. de la Torre, O. Cazalla, C. Rodriguez-Navarro, "Influence of mineralogy and firing temperature on the porosity of bricks," J. Eur. Ceram. Soc., 24 547-564 (2004).

[13]A. J. Garratt-Reed, D. C. Bell, "Energy-dispersive X-ray analysis in the electron microscope," Microscopy Handbook 49, Taylor & Francis, 2005.

[14]N. Otsu, "A threshold selection method from grey level histograms," IEEE Trans. Syst. Man Cybern, SMC-9 62-66 (1979).

[15]M. Sezgin, B. Sankur, “Survey over image thresholding techniques and quantitative performance evaluation,” J. Electron. Imaging, 13[1] 146-65 (2004).

[16]W. Burger, M. J. Burge, “Digital image processing: an algorithmic introduction using Java,” Texts in Computer Science, Springer, 2007.

[17]C. Rodriguez-Navarro, G. Cultrone, A. Sanchez-Navas, E. Sebastian, “TEM study of mullite growth after muscovite breakdown,” Am. Mineral., 88[5-6] 713-24 (2003).

[18]C. J. McConville, W. E. Lee, “Microstructural development on firing illite and smectite clays compared with that in kaolinite,” J. Am. Ceram. Soc., 88[8] 2267-2276 (2005).

[19]K. Devineau, B. Devouard, F. Villieras, F. Faure, J.-L. Devidal, A. Kohler, “Evolution of product phase assemblabes during thermal decomposition of muscovite under strong disequilibrium conditions,” Am. Mineral., 91 413-424 (2006).

[20]ASTM C67-09 “Standard test methods for sampling and testing brick and structural clay tile,” American society for Testing and Materials, 2009.

[21]ASTM D4404-84 “Standard test method for determination of pore volume and pore volume distribution of soil and rock by Mercury Intrusion Porosimetry,” American society for Testing and Materials, 2004.

[22]O. Delbrouck, J. Janssen, R. Ottenburgs, P. Van Oyen, W. Viaene, “Evolution of porosity in extruded stoneware as a function of firing temperature,” Appl. Clay Sci., 8 187-192 (1993).

[23]A. B. Abell, K. L. Willis, D. A. Lange, “Mercury Intrusion Porosimetry and image analysis of cement-based materials,” J. Colloid and Interface Sci., 211 39-44 (1999).

[24]R. Bartusch, F. Händle, “Laminations in Extrusion,” pp. 205-231 in Extrusion in Ceramics, Engineering Materials and Processes. Edited by F. Händle. Springer-Verlag Berlin Heidenberg, 2007.

[25]Ch. Hall, W. D. Hoff, “Water transport in brick, stone and concrete,” Spon Press, 2002.

[26]Y. M. Ito, M. Rosenblatt, L. Y. Cheng, F. F. Lange, A. G. Evans, "Cracking in particulate composites due to thermomechanical stress," Int. J. Fract., 17[5] 483-91 (1981).

[27]S. R. Braganca, C. P. Bergmann, H. Hübner, "Effect of quartz particle size on the strength of triaxial porcelain," J. Eur. Ceram. Soc., 26 3761-68 (2006).

[28]ASTM C39/C39M-09a, "Standard test method for compressive strength of cylindrical concrete specimens," American society for Testing and Materials, 2009.

[29]D. V. Oliveira, P. B. Lourenço, P. Roca, "Cyclic behaviour of stone and brick masonry under uniaxial compressive loading," Mater. Struct., 39[2] 219-27 (2006).

[30]W. F. Hosford, "Mechanical behavior of materials," Cambridge University Press, 2005.

[31]A. Fischer-Cripps, "Nanoindentation," Springer Verlag, New York, 2003.

[32]G. Constantinides, K. S. R. Chandran, F.-J. Ulm, K. J. Van Vliet, "Grid indentation analysis of composite microstructure and mechanics: Principles and validation," Mater. Sci. Eng. A-Struct. Mater. Properties Microstruct. Process., 430[1-2] 189-202 (2006).

[33]I. J. McColm, "Ceramic Hardness," Plenum Press, New York, 1990.

[34]W. C. Oliver, G. M. Pharr, "An improved technique for determining hardness and elastic modulus using load and displacement sensing indentation experiments," J. Mater. Res., 7[6] 1564-83 (1992).

[35]W. C. Oliver, G. M. Pharr, "Measurements of hardness and elastic modulus by Instrumented Indentation: Advances in understanding and refinements of methodology," J. Mater. Res., 19[1] 3-20 (2004).

[36]M. Vandamme, F.-J. Ulm, F. Fonollosa, "Nanogranular packing of C-S-H at substochiometric conditions," Cem. Concr. Res., 40 14-26 (2010).

[37]D. M. Titterington, A. F. M. Smith, U. E. Makov, "Statistical analysis of Finite Mixture Distributions," Wiley Series in Probability and Mathematical Statistics, John Wiley & Sons, 1985.

[38]G. J. McLachlan, D. Pell, "Finite Mixture Models," Wiley Series in Probability and Statistics, Wiley-Interscience Publication, 2000.

[39]A. P. Dempster, N. M. Laird, D. B. Rubin, "Maximum likelihood from incomplete data via the EM algorithm," J. Roy. Stat. Soc. B Met., 39 1-38 (1977).

[40]EMMIX code webpage, http://www.maths.uq.edu.au/~gjm/emmix/emmix.html.

[41]Y. Iqbal, W. E. Lee, "Fired porcelain microstructures revisited," J. Am. Ceram. Soc., 82[12] 3584-90 (1999).

[42]W. E. Lee, G. P. Souza, C. J. McConville, T. Tarvornpanich, Y. Iqbal, "Mullite formation in clays and clay-derived vitreous ceramics," J. Eur. Ceram. Soc., 28[2] 465-71 (2008).

[43]G. Schwartz, "Estimating the dimension of the model," Ann. Statist., 6[2] 461-64 (1978).

[44]P. Heyliger, H. Ledbetter, S. Kim, "Elastic constants of natural quartz," J. Acoust. Soc. Am., 114[2] 644-50 (2003).

[45]J. J. Vlassak, W. D. Nix, "Measuring the elastic properties of anisotropic materials by means of indentation experiments," J. Mech. Phys. Solids, 42 1223-1245 (1994).

[46]N. Lonnroth, Ch. L. Muhlstein, C. Pantano, Y. Yue, "Nanoindentation of glass wool fibers," J. Non-Cryst. Solids, 354[32] 3887-95 (2008).

[47]C.-C. Lin, L. Liu, "Composition dependence of elasticity in aluminosilicate glasses," Phys. Chem. Miner., 33[5] 332-46 (2006).

[48]F.-J. Ulm, M. Vandamme, H. M. Jennings, J. Vanzo, M. Bentivegna, K. J. Krakowiak, G. Constantinides, Ch. P. Bobko, K. J. Van Vliet, "Does microstructure matter for statistical nanoindentation techniques?," Cem. Concr. Compos., 32[1] 92-99 (2010).

FIGURE CAPTIONS

Figure 1. XRD spectra of B1 and B2 raw materials with phase identification.

Figure 2. XRD spectra of B1 and B2 with phase identification.

Figure 3. Typical EDX composite map of elemental composition of fired brick obtained from the tests: quartz (red), feldspar (blue), hematite (violet), aluminosilicate composite matrix (green), pocket of aluminosilicate matrix rich in alkali oxides (yellow).

Figure 4. BSE-SEM micrographs of the sample B1 (pixel aspect ratios equal to 1): a) microstructure in the section with normal vector oriented along the length of the brick (notice, the extrusion axis parallel to the longer edge of the image), characteristic coarse voids with preferential orientation along the green body extrusion direction, b) detailed view at the composite of silt particles (SP), polycrystalline-amorphous “glassy” matrix (GM) and finer porosity.

Figure 5. BSE-SEM micrographs of the sample B2 (pixel aspect ratios equal to 1): a) microstructure in the section with normal vector oriented along the length of the brick (notice, the extrusion axis normal to the plane of the image), microstructure with dominant population of finer porosity and rare coarse voids, b) detailed view at the “granular” microstructure composed of silt (SP), remnants of porous aggregates of clay (CA), early developed pockets of the “glassy” melt (GM), and porosity.

Figure 6. Typical detail of investigated microstructures exposed after chemical etching in 6% hydrofluoric acid (HF): a) sample B1 with crystals of mullite (PM-primary mullite, SM-secondary mullite) and hematite (H) , quartz (Q) and epoxy resin (E), etching time 1min, b) detailed look at the fraction of large aggregate of remnants of clay particles (CP) existing within the matrix of sample B2, regions (CP+) with apparent formation of new geometries in nanometers size from clay laths, etching time 2min.

Figure 7. Experimental cumulative distribution of the pore size measured with: a) DIA based on high resolution micrographs (B1-black, B2-red), b-c) MIP carried out in the single intrusion-extrusion cycle on the facing brick B1 (b) and common building brick B2 (c). The solid lines represent the fit with the univariate mixture model of two log-normal components obtained with Matlab. The correction for the compressibility of the system penetrometer-mercury-sample not applied.

Figure 8. Slip-lines and laminations within the plastic mass during processing in the piston extruder, adapted from Bartusch and Händle[24] with kind permission of Springer Science & Business Media.

Figure 9. Capillary water uptake: a) B1, b) B2. The axes are oriented according to the width (X), length (Y) and height (Z) directions. Note that the extrusion directions are Z for B1 and Y for B2. The apparent, small positive W-intercept at $t^{1/2}=0$ due to unsealed sides of the specimens.[25]

Figure 10. Simplified 2D scheme of the model material with capillary voids and suction of the water for two different orientations ξ_1, ξ_2 (capillary tube with uniform section model): a) material with preferential orientation of the voids, the length of the average path $\mathscr{L}_1 < \mathscr{L}_2$, the average number of capillary inlets $n_1 > n_2$, b) no alignment, distributional isotropy $\mathscr{L}_1 \approx \mathscr{L}_2$, $n_1 \approx n_2$.

Figure 11. Assessment of the mechanical properties by instrumented indentation with massive grid concept: a) indentation curves on the fictitious biphasic material, b) deconvolution of experimental data, c) the scheme of the experimental grid $l_x \times l_y$ on the surface of the material.

Figure 12. Massive Grid Indentation on sample B1: a) BSEM micrograph of local microstructure with outline of the grid N×M = 41×37, $l_x = l_y = 1.5$ μm, P = 2.25 mN, $t_{loading} = t_{unloading}$ =5 mN/min, t_{dwell} =5 sec, b) probabilistic map of mechanical phases, c) indentation imprints, d) deconvolution with Gaussians Mixture Modeling.

Figure 13. Filtering of experimental data: a,b,c) examples of abnormal load displacement curves, d) map of the identified phases with location of abnormal measurements (black phase), e) deconvolution of the grid dataset free of degenerated records.

Figure 14. Hierarchical think-model of facing clay brick B1 T≈1050°C (left) and common brick B2 microstructures T≈950°C (right).

TABLES

Table 1. Chemical composition (wt.%) of the raw materials measured with Wavelength Dispersive X-ray Fluorescence (WDXRF).

Sample	Al_2O_3	SiO_2	TiO_2	K_2O	MgO	CaO	Na_2O	Fe_2O_3	LOI
B1	19.74	60.96	0.96	2.25	0.86	1.49	0.35	5.53	7.65
B2	18.61	65.96	0.88	2.14	0.51	0.16	0.25	5.28	6.04

Components with concentration below 0.1% are excluded from the table. LOI – loss on ignition.

Table 2. Average porosity (%) measured with water immersion, MIP and DIA (values in brackets represent the coefficient of variation in %).

Sample	water immersion[1,2]	MIP[1,3]	DIA[4]
B1	21.7(5.6)	22.1(1.6)	23.1(6.1)
B2	23.4(4.9)	23.5(3.5)	22.0(8.6)

1) apparent porosity, 2) ASTM C67-09,[20] 3) ASTM D4404–84(2004),[21] 4) total porosity, size of the observation window ×100≈1238×925 μm. Min. number of samples per test Nmin=6.

Table 3. Average Young's Modulus and Compressive Strength measured at macro-scale. Note that the extrusion directions are Z for B1 and Y for B2, (values in brackets represent the coefficient of variation in %).

Sample	E_X[1]	E_Y[1]	E_Z[1]	$f_{c,X}$[2]	$f_{c,Y}$[2]	$f_{c,Z}$[2]
B1	5.4(11.6)	6.2(10.7)	8.0(5.6)	64.2(11.2)	65.3(18.7)	82.8(13.7)
B2	2.4(7.7)	3.8(3.9)	2.0(17.5)	44.2(10.4)	56.2(10.5)	42.6(8.0)
BR[3]	---	10.4(3.6)	12.7(4.4)	---	51.0(12.0)	56.8(6.4)

1) GPa, 2) MPa, 3) Brick reference Oliveira et al.[29].

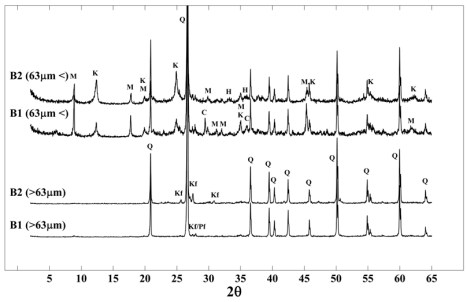

Figure 1. XRD spectra of B1 and B2 raw materials with phase identification.

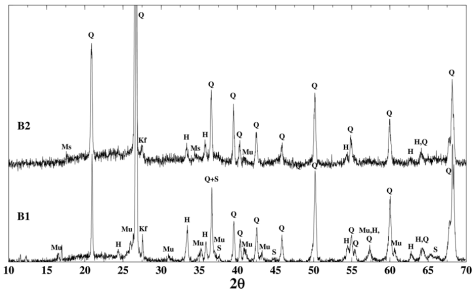

Figure 2. XRD spectra of B1 and B2 with phase identification.

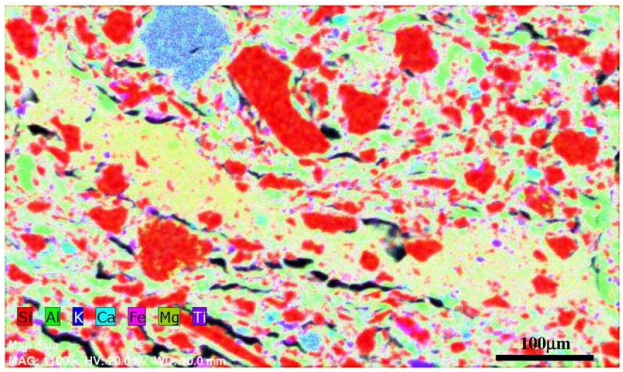

Figure 3. Typical EDX composite map of elemental composition of fired brick obtained from the tests: quartz (red), feldspar (blue), hematite (violet), aluminosilicate composite matrix (green), pocket of aluminosilicate matrix rich in alkali oxides (yellow).

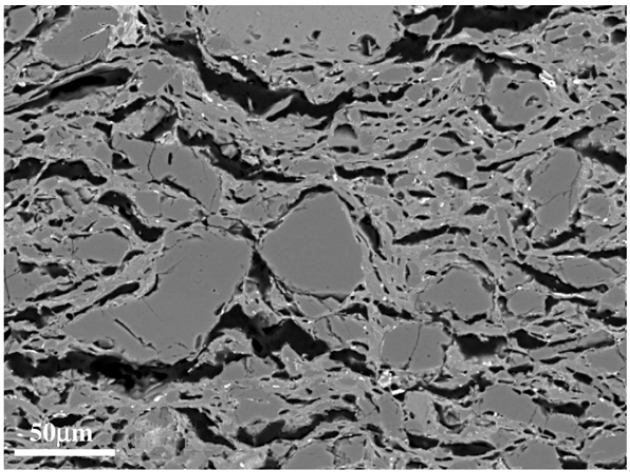

(a)

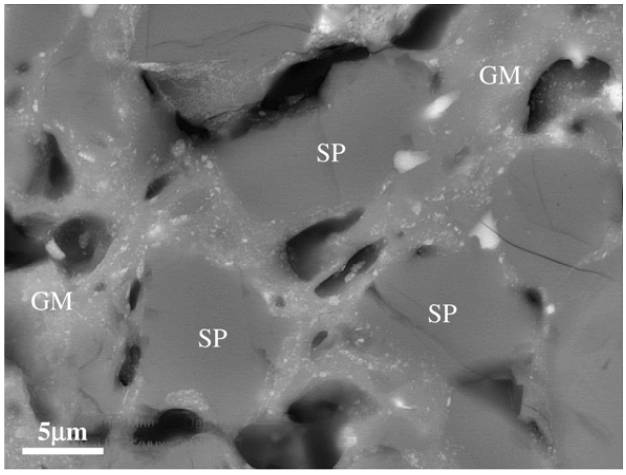

(b)

Figure 4. BSE-SEM micrographs of the sample B1 (pixel aspect ratios equal to 1): a) microstructure in the section with normal vector oriented along the length of the brick (note that the extrusion axis is parallel to the longer edge of the image), characteristic coarse voids with preferential orientation along the green body extrusion direction, b) detailed view at the composite of silt particles (SP), polycrystalline-amorphous “glassy” matrix (GM) and finer porosity.

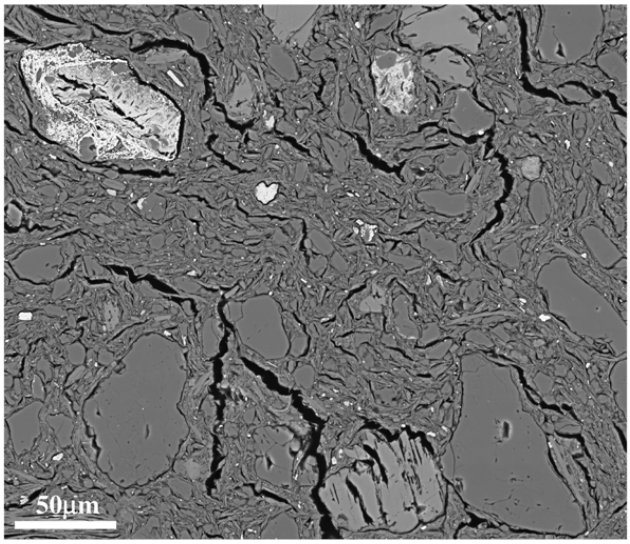

(a)

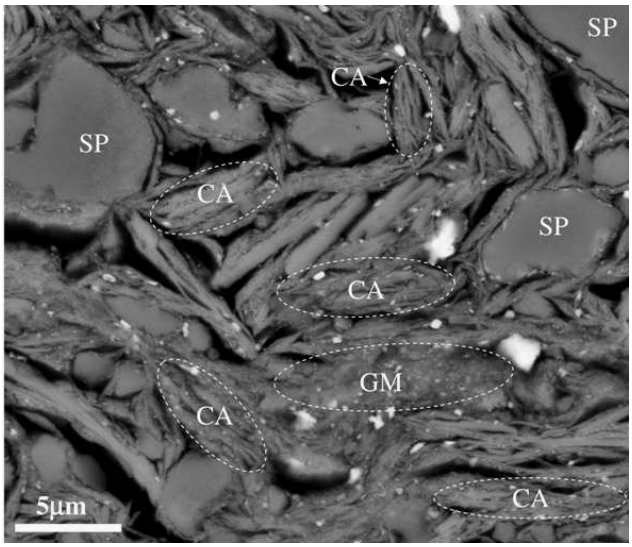

(b)

Figure 5. BSE-SEM micrographs of the sample B2 (pixel aspect ratios equal to 1): a) microstructure in the section with normal vector oriented along the length of the brick (notice, the extrusion axis normal to the plane of the image), microstructure with dominant population of finer porosity and rare coarse voids, b) detailed view at the "granular" microstructure composed of silt (SP), remnants of porous aggregates of clay (CA), early developed pocket of the "glassy" melt (GM), and porosity.

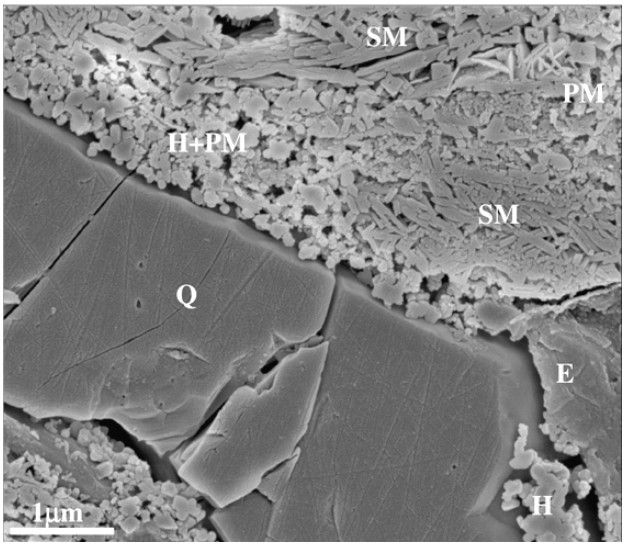

(a)

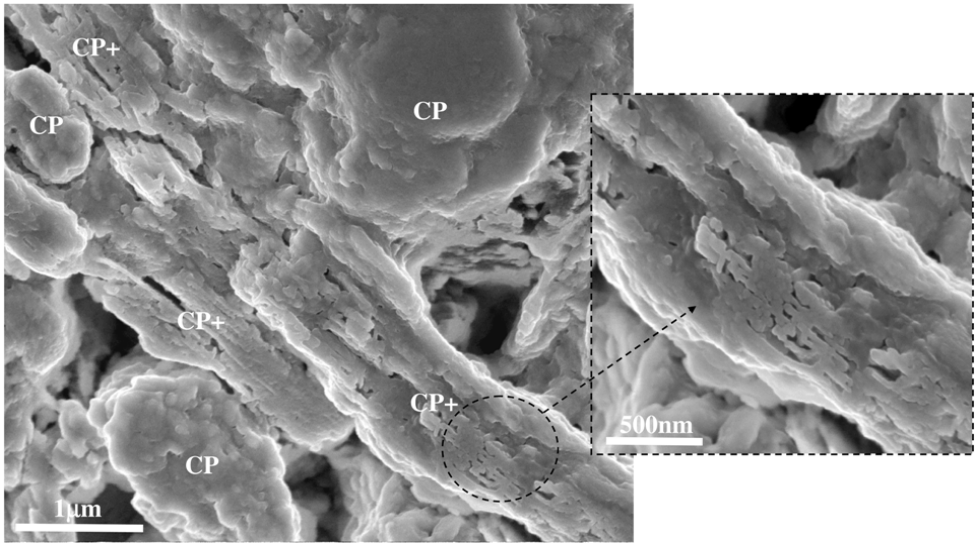

(b)

Figure 6. Typical detail of investigated microstructures exposed after chemical etching in 6% hydrofluoric acid (HF): a) sample B1 with crystals of mullite (PM-primary mullite, SM-secondary mullite) and hematite (H) , quartz (Q) and epoxy resin (E), etching time 1min, b) detailed look at the fraction of large aggregate of remnants of clay particles (CP) existing within the matrix of sample B2, regions (CP+) with apparent formation of new geometries in nanometers size from clay laths, etching time 2min.

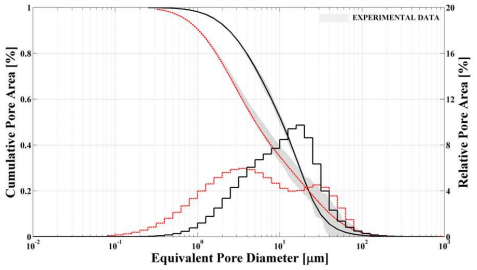

(a)

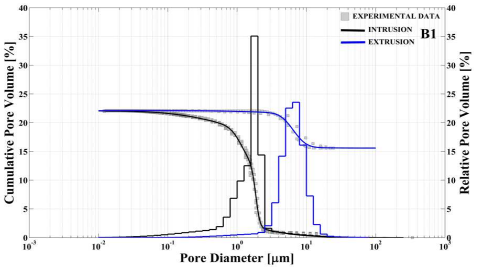

(b)

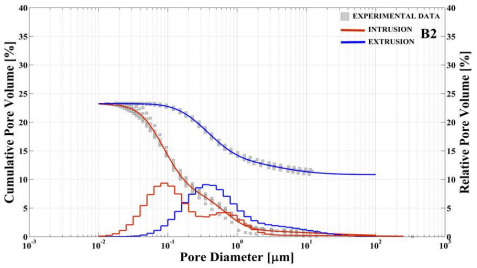

(c)

Figure 7. Experimental cumulative distribution of the pore size measured with: a) DIA based on high resolution micrographs (B1-black, B2-red), b-c) MIP carried out in the single intrusion-extrusion cycle on the facing brick B1 (b) and common building brick B2 (c). The solid lines represent the fit with the univariate mixture model of two log-normal components obtained with Matlab. The correction for the compressibility of the system penetrometer-mercury-sample not applied.

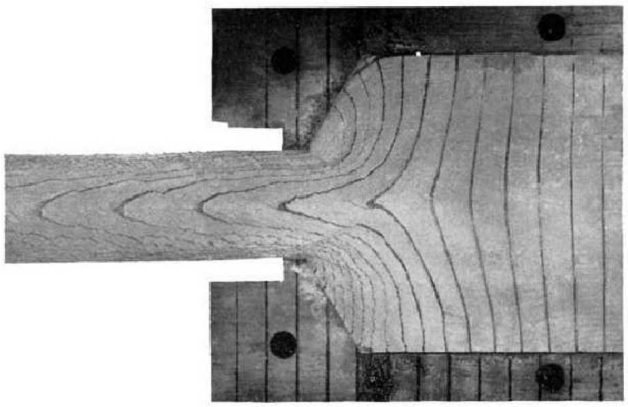

Figure 8. Slip-lines and laminations within the plastic mass during processing in the piston extruder, adapted from Bartusch and Händle[24] with kind permission of Springer Science & Business Media.

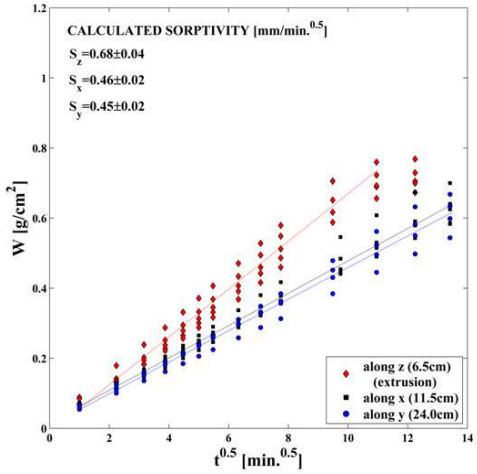

(a)

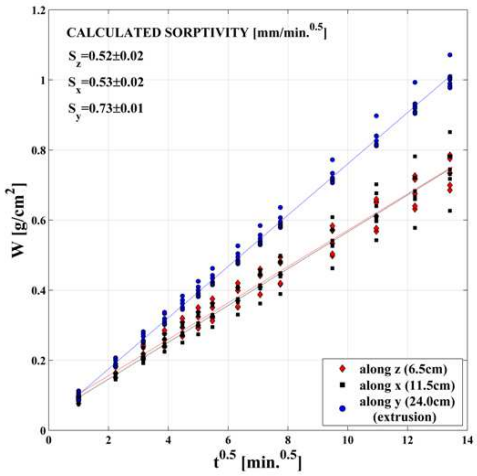

(b)

Figure 9. Capillary water uptake: a) B1, b) B2. The axes are oriented according to the width (X), length (Y) and height (Z) directions. Note that the extrusion directions are Z for B1 and Y for B2. The apparent, small positive W-intercept at $t^{1/2}=0$ due to unsealed sides of the specimens.[25]

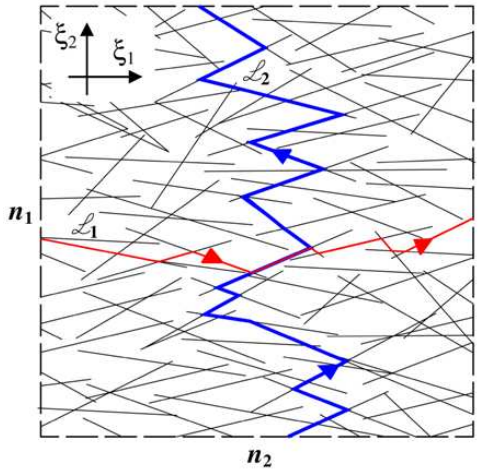

(a)

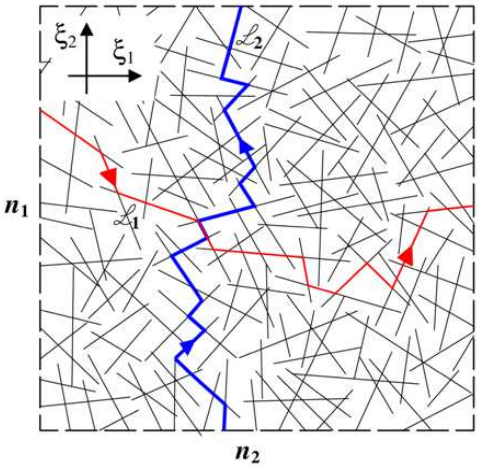

(b)

Figure 10. Simplified 2D scheme of the model material with capillary voids and suction of the water for two different orientations ξ_1, ξ_2 (capillary tube with uniform section model): a) material with preferential orientation of the voids, the length of the average path $\mathscr{L}_1<\mathscr{L}_2$, the average number of capillary inlets $n_1>n_2$, b) no alignment, distributional isotropy $\mathscr{L}_1\approx\mathscr{L}_2$, $n_1\approx n_2$.

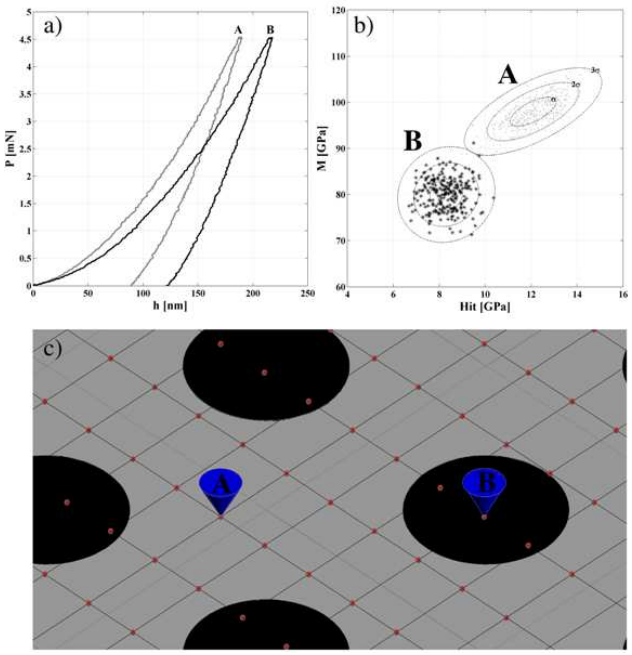

Figure 11. Assessment of the mechanical properties by instrumented indentation with massive grid concept: a) indentation curves on the fictitious biphasic material, b) deconvolution of experimental data, c) the scheme of the experimental grid $l_x \times l_y$ on the surface of the material.

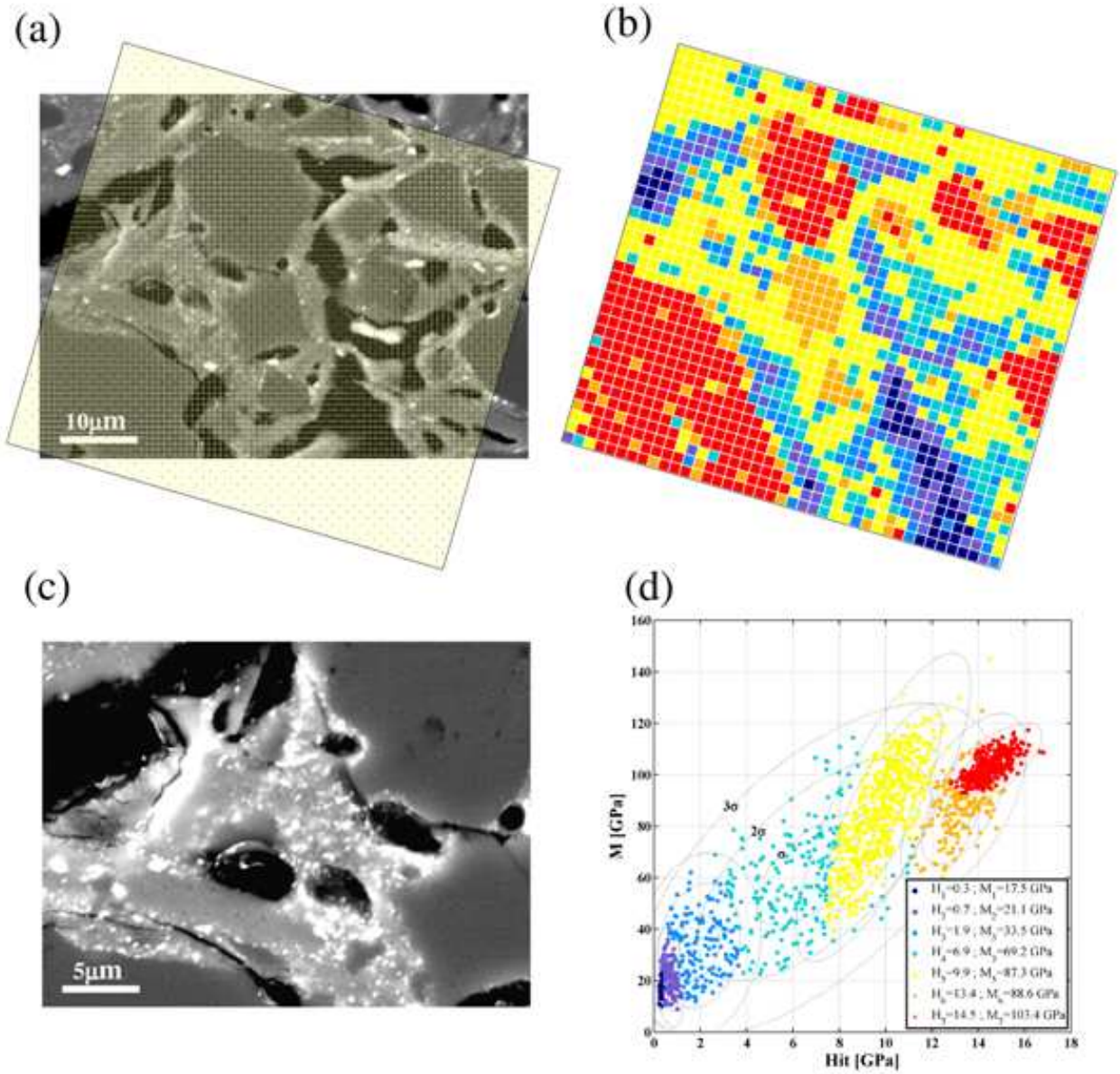

Figure 12. Massive Grid Indentation on sample B1: a) BSEM micrograph of local microstructure with outline of the grid N×M = 41×37, l_x = l_y = 1.5 µm, P = 2.25 mN, $t_{loading}$ = $t_{unloading}$ =5 mN/min, t_{dwell} =5 sec, b) probabilistic map of mechanical phases, c) indentation imprints, d) deconvolution with Gaussians Mixture Modeling.

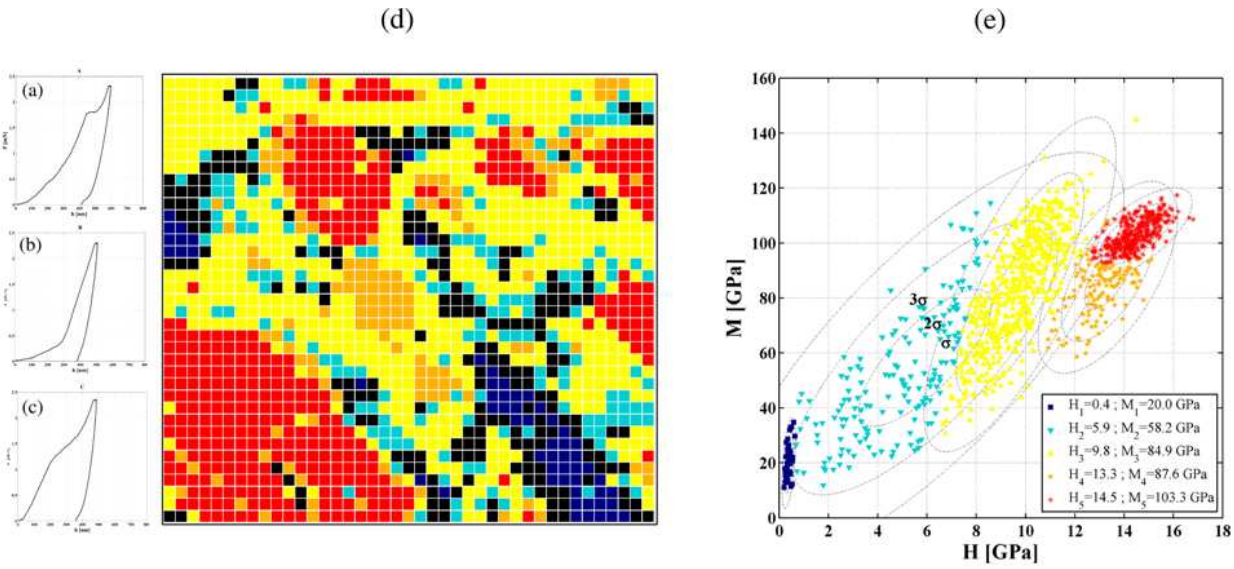

Figure 13. Filtering of experimental data: a,b,c) examples of abnormal load displacement curves, d) map of the identified phases with location of abnormal measurements (black phase), e) deconvolution of the grid dataset free of degenerated records.

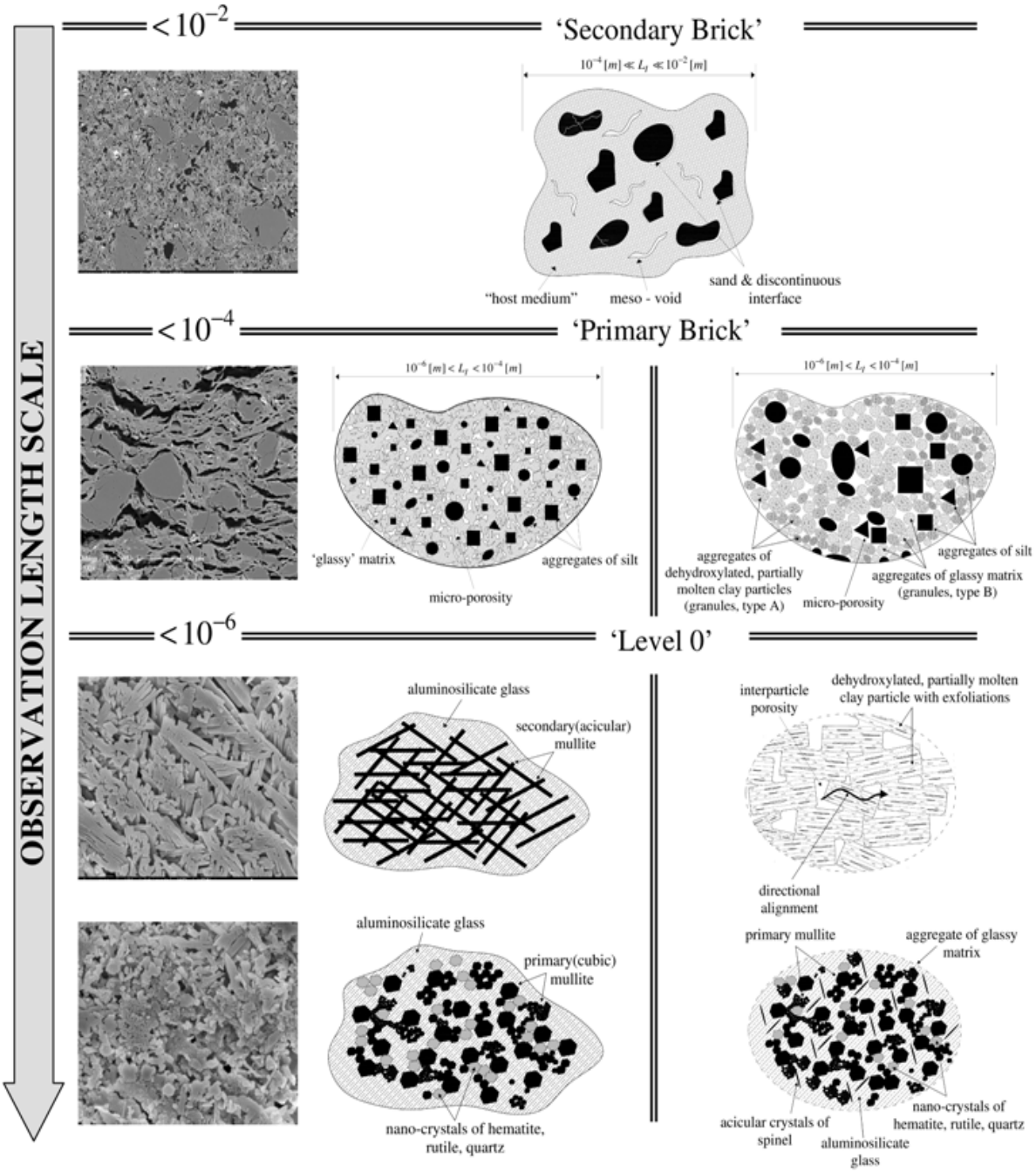

Figure 14. Hierarchical think-model of facing clay brick B1 T≈1050°C (left) and common brick B2 microstructures T≈950°C (right).